Structure
Article

Structural Polymorphism of the ParM Filament and Dynamic Instability

Vitold E. Galkin,[1,*] Albina Orlova,[1] Chris Rivera,[2] R. Dyche Mullins,[2] and Edward H. Egelman[1,*]
[1]Department of Biochemistry and Molecular Genetics, University of Virginia, Charlottesville, VA 22908-0733, USA
[2]Department of Cellular and Molecular Pharmacology, UCSF Medical School, San Francisco, California 94107, USA
*Correspondence: egelman@virginia.edu (E.H.E.), galkin@virginia.edu (V.E.G.)
DOI 10.1016/j.str.2009.07.008

SUMMARY

Segregation of the R1 plasmid in bacteria relies on ParM, an actin homolog that segregates plasmids by switching between cycles of polymerization and depolymerization. We find similar polymerization kinetics and stability in the presence of either ATP or GTP and a 10-fold affinity preference for ATP over GTP. We used electron cryo-microscopy to evaluate the heterogeneity within ParM filaments. In addition to variable twist, ParM has variable axial rise, and both parameters are coupled. Subunits in the same ParM filaments can exist in two different structural states, with the nucleotide-binding cleft closed or open, and the bound nucleotide biases the distribution of states. The interface between protomers is different between these states, and in neither state is it similar to F-actin. Our results suggest that the closed state of the cleft is required but not sufficient for ParM polymerization, and provide a structural basis for the dynamic instability of ParM filaments.

INTRODUCTION

Bacterial survival in an environment containing fungi and heavy metal ions depends on plasmids—extrachromosomal DNA molecules capable of replicating independently of the host genome. High-copy-number plasmids are separated randomly in bacteria, whereas low-copy-number plasmids require an active mechanism of segregation to preserve the maintenance of plasmids in daughter cells following division. Most of our knowledge about plasmid DNA partitioning comes from studies on the large low-copy-number plasmid R1 (Nordstrom et al., 1980). The stability operon *par* encodes three components sufficient for plasmid segregation: *parR* and *parM* genes along with the *cis*-acting locus, *parC* (Gerdes and Molin, 1986). The current model for type II partitioning assumes that ParR binds cooperatively to several repeats of the *parC* locus, whereas ParM bound to ParR pushes the two newly formed plasmids to the opposite poles of the bacterial cell via ATP-dependent polymerization (Moller-Jensen et al., 2003; Salje and Lowe, 2008; Campbell and Mullins, 2007; Choi et al., 2008). Sequence analysis of ParM (Jensen and Gerdes, 1997) has revealed a set of common conserved residues found in the actin superfamily of proteins (Bork et al., 1992), whereas the crystal structure of ParM unambiguously showed ParM to be a bacterial actin homolog (van den Ent et al., 2002). Nevertheless, alignment of the crystal structures of actin and ParM reveals that regions of actin involved in subunit-subunit interactions within the filament (Oda et al., 2009) are very different from ParM (van den Ent et al., 2002). This coincides with the finding that, in contrast to the F-actin right-handed two-start helix, ParM forms a left-handed two-start helix (Orlova et al., 2007; Popp et al., 2008) caused by the different subunit-subunit interfaces. It is likely that the structural differences in filament organization between F-actin and ParM result in the substantial differences observed between the polymerization properties of these proteins. ParM nucleates 300 times faster than actin and grows from both ends with the same rate (Garner et al., 2007). Importantly, ParM filaments are dynamically unstable and, upon ATP hydrolysis, can switch from elongation to rapid shortening (Garner et al., 2004). Such instability is crucial for plasmid partitioning, as ParM mutants with reduced ATPase activity in vitro are nonfunctional in vivo (Jensen and Gerdes, 1997). The filaments capped with the ParR/ParC complex are stable and can grow to be long in the cell (Campbell and Mullins, 2007). The ParR/ParC complex may bind to the side of ParM and remain attached to the ATP cap of the growing filament, preventing the dissociation of the cap (Choi et al., 2008). Alternatively, the ParR/ParC complex may form a protective cap on the end of the filament to maintain its integrity via a processive polymerization mechanism (Salje and Lowe, 2008).

However, the structure of the ParM filament is still controversial, and it has been suggested that the intersubunit contacts in ParM are similar to those in F-actin (Popp et al., 2008; Lowe and Amos, 2009). We show that the ParM filament has both variable twist and variable axial rise, and subunits can coexist within the same filament in two structural states, with the nucleotide cleft closed or open. These states are not simply related to the bound nucleotide, as both states may be found with the same nucleotide bound. However, the nucleotide biases the distribution of states, with ATP shifting the distribution toward the closed state while ADP-Pi shifts the equilibrium toward the open form.

RESULTS

Comparison of Negatively Stained and Frozen Hydrated ParM Filaments Formed in the Presence of AMP-PNP and GMP-PNP

A recent paper (Popp et al., 2008) has used X-ray fiber diffraction and negative stain EM to study ParM filaments and arrived at

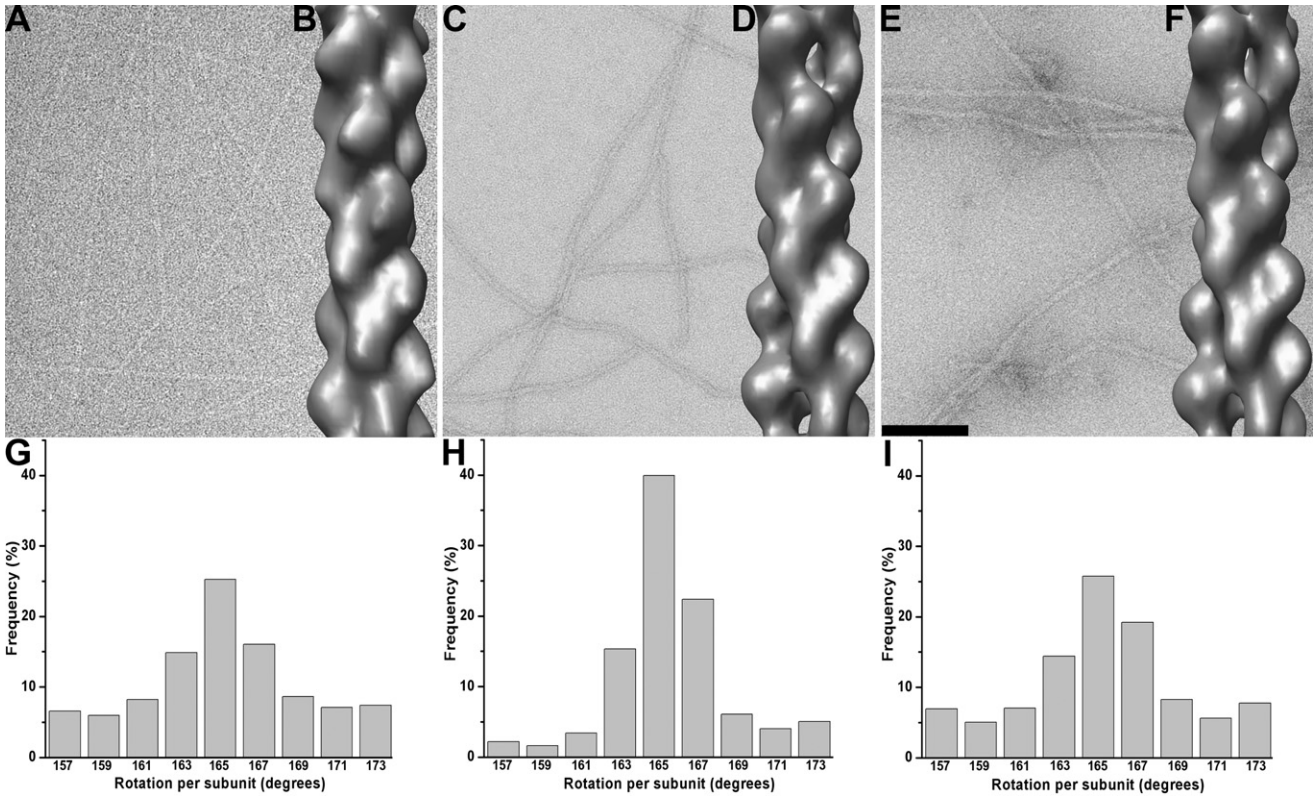

Figure 1. EM Images of ParM Filaments in the Presence of AMP-PNP and GMP-PNP with Corresponding Global Reconstructions and Twist Distributions

(A) Frozen hydrated and (C) negatively stained ParM filaments polymerized in the presence of AMP-PNP.

(E) Same as (C), but with GMP-PNP rather than AMP-PNP.

The global 3D reconstructions derived from the segments in (A, C, and E) are shown as solid surfaces in (B, D, and F), respectively. Twist distributions of frozen hydrated (G) and negatively stained (H) AMP-PNP ParM filaments.

(I) Twist distribution of the GMP-PNP negatively stained ParM. The scale bar in (E) is 1,000 Å.

very different results from the cryo-EM structure that we published (Orlova et al., 2007). Since Popp et al. (2008) used GMP-PNP (a nonhydrolyzable analog of GTP) while we used AMP-PNP (a nonhydrolyzable analog of ATP) for our studies, we performed an extensive analysis of the cryo-EM as well as negatively stained ParM filaments formed in the presence of AMP-PNP or GMP-PNP (Figure 1). The overall reconstruction of the ParM-AMP-PNP filaments from cryo-EM (Figure 1B) was very similar to that derived from the negatively stained filaments (Figure 1D). Unexpectedly, we found that the new reconstruction of cryo-EM ParM-AMP-PNP filaments (Figure 1B) was significantly different from the original reconstruction (Orlova et al., 2007). The nucleotide-binding cleft was closed (Figure 1B), similar to that observed in the negatively stained reconstructions (Figures 1D and 1F). An examination of the original data revealed a mistake in the way the Contrast Transfer Function (CTF) was corrected in those images. This led to an error in the phases of the images, resulting in an artifactual reconstruction.

Negatively stained ParM filaments formed in the presence of AMP-PNP (Figure 1C) look similar to the filaments polymerized in the presence of GMP-PNP (Figure 1E), which is consistent with the similarity of the two respective overall reconstructions (Figures 1D and 1F). Both reconstructions are similar to the reconstruction of ParM-GMP-PNP filaments from Popp et al. (2008). The only difference that we observe between the negatively stained filaments is a slight increase in the twist heterogeneity in the presence of GMP-PNP (Figure 1I), compared with that found in the presence of AMP-PNP (Figure 1H). In the presence of AMP-PNP, we observed a slight increase in the variance of twist in the cryo set (Figure 1G), compared with that found with negative stain (Figure 1H), but this may reflect a lower signal-to-noise ratio in the frozen hydrated sample.

Solution Studies with ATP versus GTP

In agreement with Popp et al. (2008), we find that the addition of GTP induces polymerization of ParM filaments. To rule out any effects of labeling with fluorescent dyes, we used unlabeled ParM and monitored polymerization by light scattering. At steady state, the apparent critical concentrations of GTP and ATP ParM are approximately equal (not shown). To determine the affinities of ParM for ATP and GTP, we performed competition binding experiments using a fluorescent derivative of ATP (etheno-ATP). To prevent polymerization during the experiment, we used a ParM concentration of 0.4 μM, well below the ATP critical concentration. Competition with unlabeled ATP yielded a dissociation equilibrium constant of 0.9 μM, which is somewhat

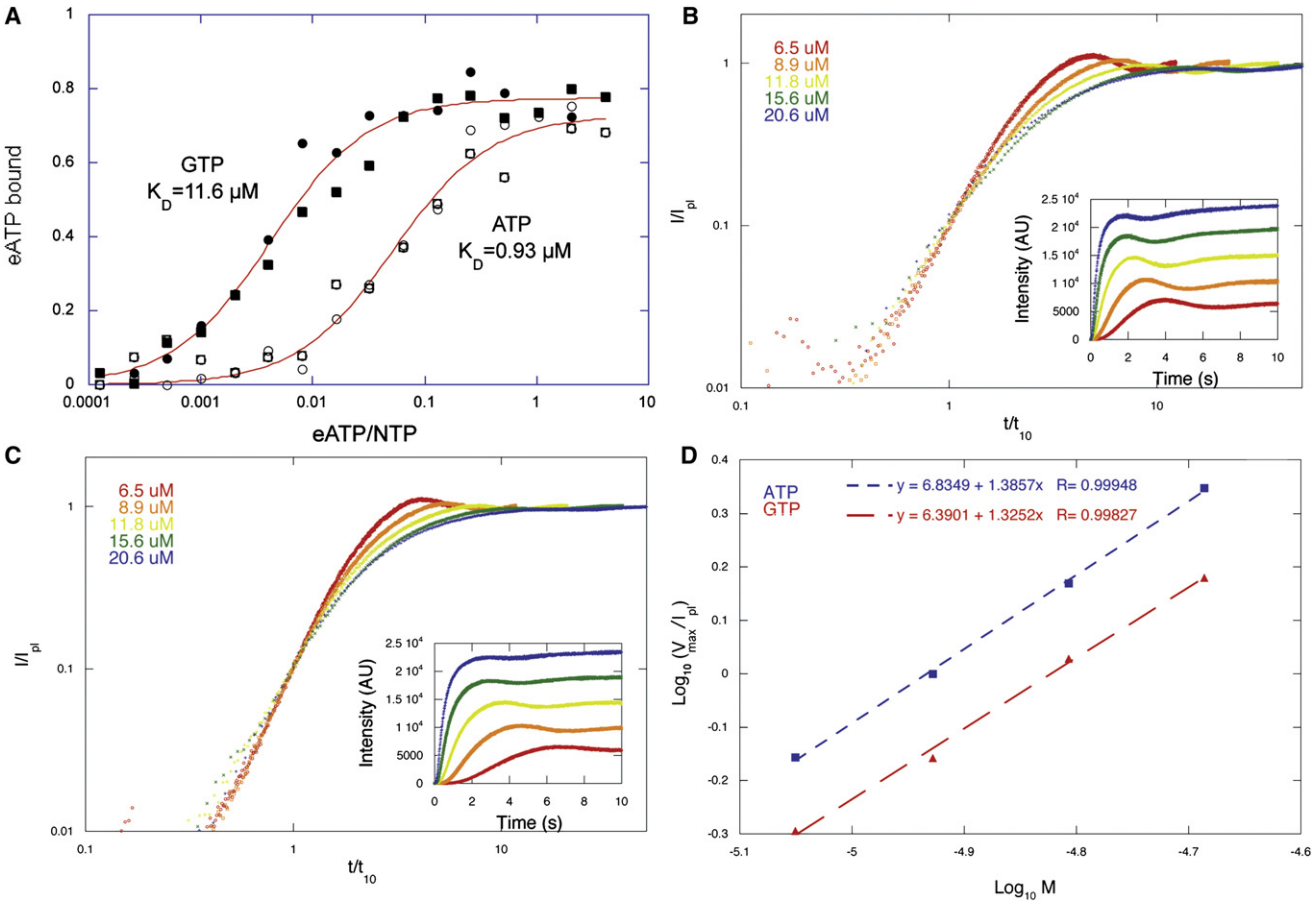

Figure 2. ParM Accommodates ATP and GTP

(A) Competition of etheno-ATP away from ParM by ATP and GTP. The affinity of ParM for ATP (K_d = 0.9 μM) is more than 10-fold higher than for GTP (K_d = 11.6 μM). The experiment was performed three times with identical results. Conditions: Buffer: 100 mM KCl, 1 mM $MgCl_2$, 10 mM HEPES (pH 7.0). Temperature: 24°C.

(B) Assembly of five different concentrations of R1 ParM initiated by addition of 5 mM ATP.

(C) Assembly of the same concentrations of ParM initiated by addition of 5 mM GTP. Polymerization was monitored by right angle light scattering and the amplitude of the light scattering signal normalized to the value at plateau. Time scales were normalized to the time required to reach 10% of the plateau value. Insets: raw data before normalization. The similarity of the slopes of the curves at early time points indicates that, in each case, the nucleation mechanism is the same at all concentrations tested.

(D) Log-log plot of the normalized maximum velocity of polymerization versus ParM concentration. The identical slopes argue that the mechanism of nucleation is the same in both cases. The offset between the lines suggests that spontaneous nucleation is slightly faster in the presence of ATP.

weaker than the affinity we measured for etheno-ATP (Garner et al., 2004). Competition with GTP yielded a value of 11.6 μM, indicating that, as in all other actin family proteins studied to date, the nucleotide binding pocket of ParM accommodates ATP more readily than GTP (Figure 2A).

In rapid mixing experiments at high nucleotide concentrations (5 mM), GTP-ParM filaments assemble rapidly and spontaneously (Figures 2B and 2C) but slightly more slowly than ATP-ParM filaments. The rate of polymer assembly at early time points and the concentration dependence of the maximum rate of assembly (Figure 2D) both indicate that GTP ParM assembles via the same mechanism as ATP ParM and with the same apparent nucleus size of 3 monomers (Flyvbjerg et al., 1996; Nishida and Sakai, 1983). The slower rate of assembly of GTP filaments is consistent with a slower rate of spontaneous nucleation or a slower rate of nucleotide association.

In low concentrations of nucleotide (below 0.5 mM), GTP ParM filaments assemble and spontaneously disassemble in a manner similar to ATP filaments (Figure 3), suggesting that they exhibit a similar nucleotide hydrolysis-dependent dynamic instability. To investigate the polymer dynamics of GTP ParM filaments more carefully, we used total internal reflection fluorescence (TIRF) microscopy of Alexa-488-labeled ParM filaments. Under conditions in which we can observe individual filaments, GTP ParM behaves identically to ATP ParM (Figures 3E and 3F). First we remeasured the dynamics of ATP ParM filaments and obtained rate constants for elongation and catastrophic shortening of $2.9 \pm 0.8\ \mu M^{-1}\ s^{-1}$ (n = 7) and $149 \pm 63\ s^{-1}$ (n = 5), respectively. These values are within a factor of two of those we measured previously (Garner et al., 2004). Like ATP filaments, GTP filaments elongate symmetrically with the same rate constant ($2.7 \pm 0.8\ \mu M^{-1}\ s^{-1}$; n = 16) at each end. After a period of steady

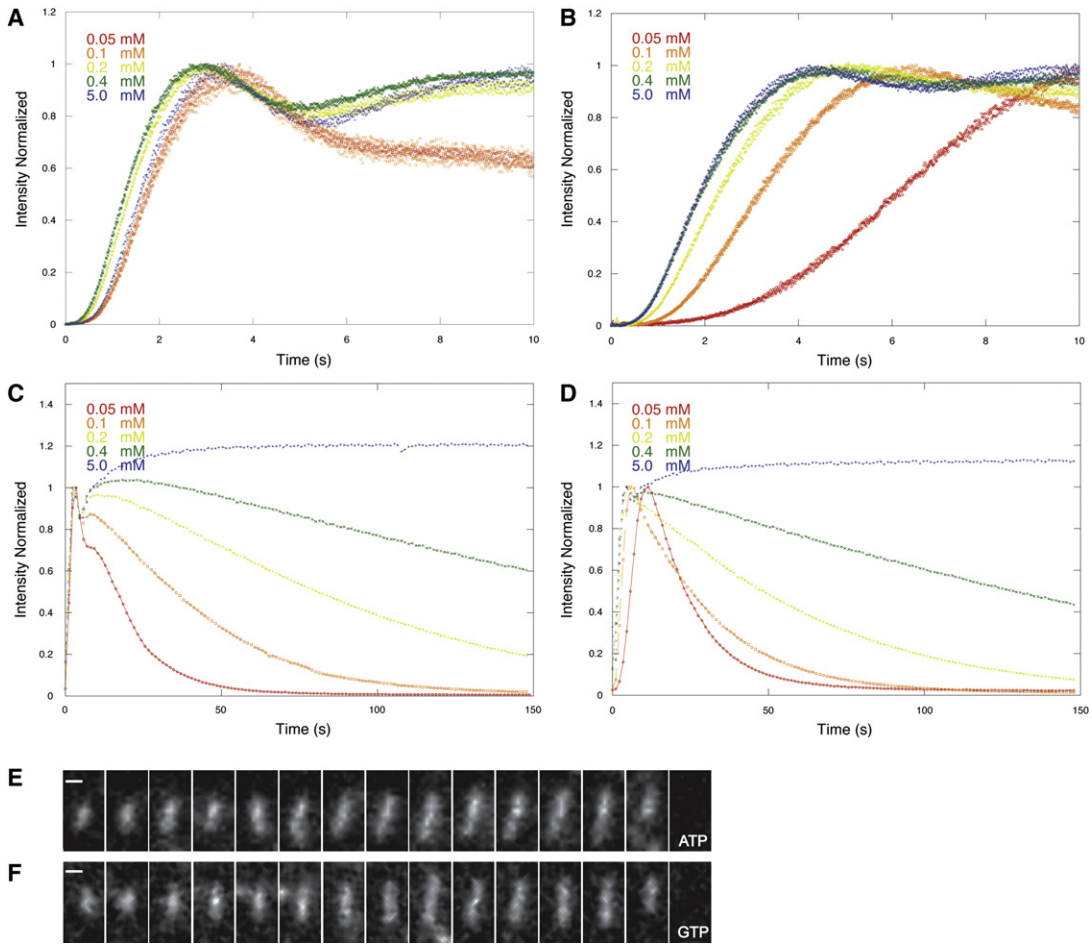

Figure 3. Effects of Varying Nucleotide Concentration on Assembly and Stability of R1 ParM Filaments

Polymerization of 10 μM R1 ParM was initiated by addition of varying amounts of ATP (A, C) or GTP (B, D). For all concentrations between 0.05 mM and 5 mM, polymer content reached its maximum value within 10 s (A, B). The initial phase of assembly was less sensitive to variations in the concentration of ATP (A) compared to GTP (B), suggesting that the association of GTP is slower than that of ATP. Once assembled, ParM polymer has similar stability at the same concentrations of ATP and GTP (C, D). In 5 mM ATP (C) or GTP (D), the polymer content remains constant for many minutes. At concentrations below 0.5 mM, the polymer content decreases significantly within 150 s, and, at concentrations below 0.1 mM, polymer completely disappears within 120 s. TIRF microscopy of ParM filaments assembled in ATP (E) or GTP (F). The rates of elongation and disassembly of individual filaments are identical under the two conditions.

elongation, GTP filaments also switch to a phase of rapid shortening with the same rate of disassembly as that of ATP ParM ($135 \pm 63\ s^{-1}$; n = 5) (Figure 3F). Upon switching from elongation to shortening, both ATP and GTP filaments disassemble completely. We never observe rescue of shortening ParM filaments either in the presence of ATP (Garner et al., 2004) or GTP (present study). These results differ substantially from those of Popp et al. (2008), and we discuss the discrepancies below.

Symmetry of the Filaments

One of the main arguments that Popp et al. (2008) made for our original ParM filament model being wrong is that we assigned a symmetry to our filament model that does not match the observed X-ray fiber diffraction patterns. Popp et al. (2008) describe the symmetry of their ParM filaments as having 37 subunits in 17 turns of the one-start helix. The repeat, the distance needed to translate a subunit along the axis so that it is in register with another subunit, would be 37*(24.5 Å) = 900, where 24.5 Å is the axial rise per subunit. We have argued (Egelman, 2007) that the description of helical symmetry in terms of a repeat is a poor one, as there is no reason that the symmetry of a helical polymer can be best represented by the ratio of relatively small integers. For a helix having a 37/17 symmetry, the rotation between adjacent subunits would be 360°*17/37, or 165.4°. Consider an almost infinitesimal change in the twist of this structure by 0.04° per subunit. The symmetry is now best approximated as having 3,701 subunits in 1,700 turns, with a repeat of 90,675 Å. It is therefore much more useful to simply describe the angle of rotation between subunits, which is a continuously variable parameter.

Popp et al. (2008) state that we assigned a symmetry of 31 subunits in 14 turns (162.6°) to our ParM filament model. This is untrue. The header of the PDB file (2QU4) for our ParM model that we deposited and that they used for their simulations states that the rotation needed to generate a filament is 165.4° (the same rotation that they describe). We stated in the text of our

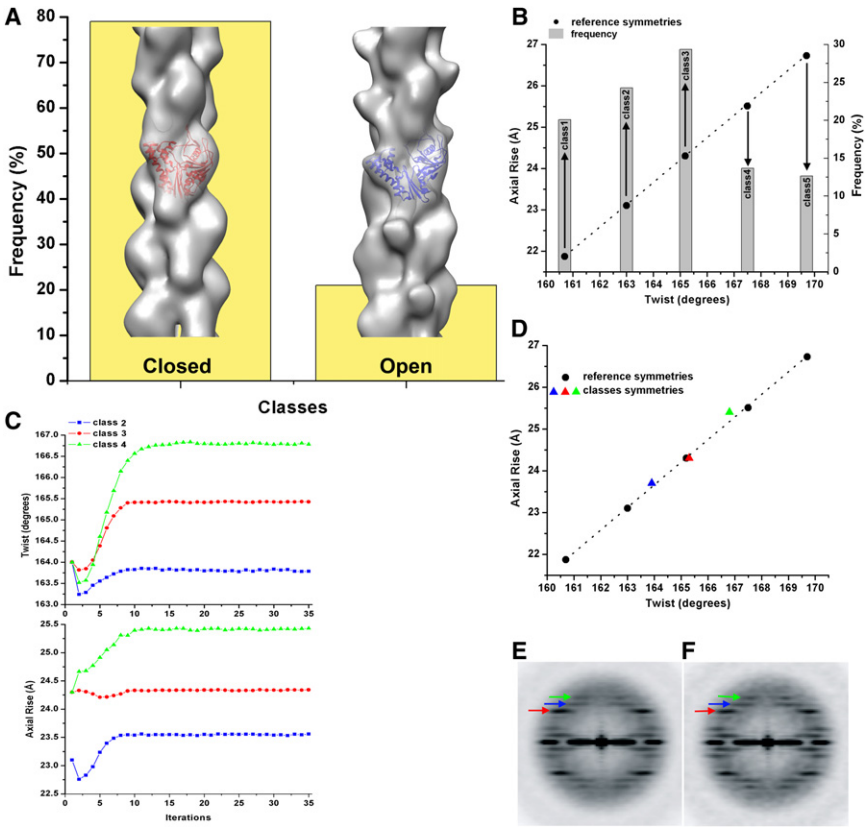

Figure 4. Sorting of Frozen Hydrated ParM Filaments by Both the Structural State and the Helical Symmetry

(A) Closed crystal structure (red ribbons, PDB 1MWM) and the open crystal structure (blue ribbons, PDB 1MWK) were used to generate two reference models (solid surfaces). These models were used to sort out short segments of ParM into classes based on the opening of the nucleotide-binding cleft (yellow bins).

(B) Five reference models were designed (see Experimental Procedures) to classify closed-cleft segments on the basis of their twist and axial rise. Frequency counts of observed filament segments are shown as gray bins, while black circles represent the corresponding class symmetry.

(C) Convergence of classes of images from (B) in the IHRSR procedure validates the sorting shown in (B).

(D) The stable solutions after convergence (C) show a strong coupling between the twist and the axial rise. Power spectrum of all closed-cleft segments (E) is compared with the power spectrum from class3 (F), the largest class in (B). Three layer lines are marked with arrows: n = 3 is red, n = 1 is blue, and n = −1 is green. The layer lines from the one-start helices are stronger in (F) than they are in the global average (E), due to reduced heterogeneity after the symmetry sorting.

paper that in the ParM filament the rotation between every other subunit "is on average approximately −29°," which would be a rotation of 165.5° between subunits. The consequence of this error in the description of our filament symmetry was that the R-factor between our model and their observed X-ray fiber diffraction pattern was great (0.68), but much of this R-factor simply arises from comparing diffraction patterns having two different sets of spacings. Attempting to match our new three-dimensional reconstruction and filament model with their observed X-ray fiber diffraction pattern (Popp et al., 2008) has revealed that ParM filaments cannot be described by a single structural state. In fact, we can now show that globally averaged diffraction patterns from ParM filaments, whether from X-ray scattering or cryo-EM, represent a sum of two states.

Subunits in the ParM Filament Can Exist in Two Different Structural States

The global reconstructions of ParM shown in Figures 1B, 1D, and 1F, as well as from the Maeda group (Popp et al., 2008), are best fit by a subunit having a closed nucleotide-binding cleft. Since ParM has been crystallized in both closed and open forms (van den Ent et al., 2002), we designed two reference volumes composed of protomers having their clefts either closed or open and arranged into filaments having the same helical symmetry as the global reconstruction (Figure 1B). Surprisingly, almost 20% of segments had the higher correlation with the model having its cleft open (Figure 4A). The reconstructions derived from these two classes (Figure 4A) validated the sorting—no perturbations from the crystal structures of the closed and open states of ParM were needed to fit the crystals into the closed and the open reconstructions (filtered to ~20 Å resolution), respectively. The sorting did not introduce any bias into the reconstructions, as both sets of images after sorting were reconstructed using the Iterative Helical Real Space Reconstruction (IHRSR) method (Egelman, 2000) starting from a featureless solid cylinder as an initial model. The IHRSR method has been shown to offer many advantages in the three-dimensional reconstruction of helical polymers that are disordered or heterogeneous (Egelman, 2007). We checked whether segments classified as being in different states came from different filaments, or could be found within the same filaments, by examining the ten longest filaments in our images (data not shown). The conclusion was that all variation (within statistical sampling) was within filaments, and not between filaments.

Previously, we showed that, like F-actin (Egelman and DeRosier, 1982), ParM filaments have a variable twist (Orlova et al., 2007). Surprisingly, sorting by the twist did not improve the resolution of the closed ParM reconstruction (data not shown), suggesting that, in addition to the variable twist, ParM may have other sources of heterogeneity, such as a variable axial rise. The power spectrum of the closed ParM set had a very strong n = 3 layer line (Figure 4E, red arrow), while the reflections from the right and left handed one-start helices were significantly weaker (Figure 4E, blue and green arrows respectively). The power spectrum from the projection of the reconstruction, however, showed significantly stronger one-start layer lines (Figure 5E, blue and green arrows), revealing a discrepancy with the power spectrum from the images used to generate the

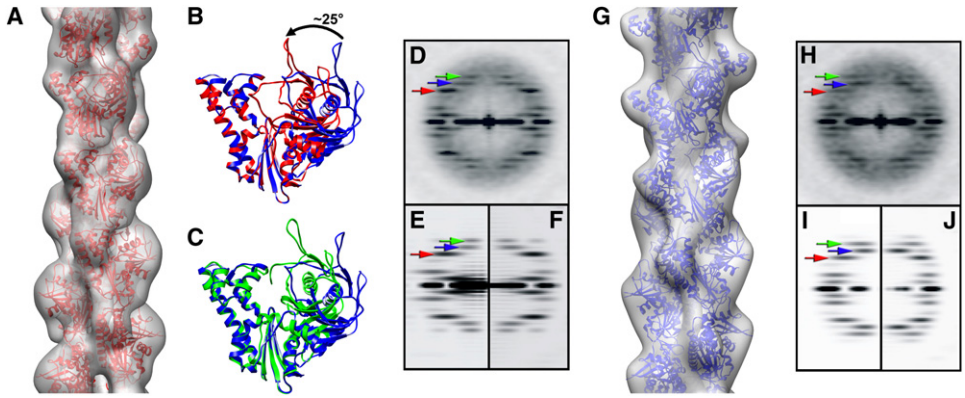

Figure 5. The Two Pseudo-Atomic Models of the ParM Filament

(A) Reconstruction of the ParM filament in the closed state is filtered to 17 Å resolution, and the corresponding atomic model is shown as red ribbons.

(B) The two domains of the APO crystal structure of ParM (blue ribbons) have to be moved toward each other by ~25° (red ribbons) to achieve a better fit to the closed state filament (see text for details).

(C) The same closing of the nucleotide binding cleft is observed between the APO (blue ribbons) and ADP-bound (green ribbons) crystal structures.

(D–F) Power spectra generated from the raw images (D), and projections of either the three-dimensional reconstruction (E) or the corresponding atomic model of the closed filament (F). Three layer lines are marked with arrows: n = 3 is red, n = 1 is blue, and n = −1 is green.

(G–J) (G) Three-dimensional reconstruction of the ParM filament in the open state is filtered to 19 Å resolution, and the corresponding atomic model is shown as blue ribbons. Power spectra generated from the raw images (H), and projections of either the three-dimensional reconstruction (I) or the corresponding atomic model of the open filament (J). Three layer lines are marked with arrows as in (E).

reconstruction (Figure 4E). A reasonable explanation is that the pitch of the three-start helix is less variable than the pitch of the one-start helices, and such variability would blur the reflections in the averaged power spectrum. The fall in the intensities of layer lines due to the helical disorder has been quantitatively described for F-actin and other helical filaments (Egelman and DeRosier, 1982). Reconstructing with the IHRSR method, on the other hand, would tend to align the one-start helices in spite of their variability, accounting for the discrepancy. To check this possibility, we designed five models with a fixed three-start helical pitch, but with both variable twist and axial rise (see Experimental Procedures). The frequency distribution from such a sorting is shown in Figure 4B. The classes 2, 3, and 4 were used in the IHRSR procedure and converged to the expected symmetry parameters (Figures 4C and 4D). To validate the sorting independently from the IHRSR method, we calculated the power spectra for these three classes (see Movie S1 available online). As expected, the position of the three-start helix layer line in each power spectrum was fixed, whereas n = 1 and n = −1 layer lines positions moved as predicted. A power spectrum from the largest single class (Figure 4F) shows an enhancement of these one-start layer lines when compared to the average of the five classes (Figure 4E), as expected. Thus, there is a very strong correlation between the twist and the axial rise (Figure 4D), and both show significant variation in ParM filaments.

An obvious question is whether the variability in axial rise could actually be coming from variations in magnification, or from filaments that are tilted out of the plane of the image. If changes in magnification were responsible, then we would see filament reconstructions with different diameters, and we would see shifts in the radial positions of layer line peaks in the power spectra (Movie S1). Such changes are not seen. Further, the determination of twist is independent of magnification, so we would see no correlation between twist and axial rise, but we see a strong correlation, eliminating the possibility that our results can be explained by variable magnification. If the differences in axial rise were due to out-of-plane tilt, then a tilt of ~23° would be needed to explain a change in axial rise from 25.5 Å to 23.5 Å. Since the filaments are imaged after adsorption to a carbon support film and do not lie over holes, this possibility seems extremely unlikely. Our results unambiguously show that, in addition to the variable twist, ParM has a variable axial rise, and that the twist and the axial rise are coupled. We therefore used this new sorting to generate an improved three-dimensional reconstruction of the closed state of the ParM filament, using the largest class (class3, n = 3,116 segments). We did not attempt to sort out the helical heterogeneity in the open ParM state because of the more limited number of total segments (n = 3,374).

The two reconstructions are shown as transparent surfaces in Figures 5A and 5G. To determine the resolution of the map in each case, we used a procedure described in (Galkin et al., 2008), which returned the most pessimistic estimation of the resolution of ~17.2 Å for the closed state reconstruction (after sorting for the variable twist and rise) and ~19.5 Å for the open state (no sorting for twist and rise). No perturbations of the crystal structure of ParM in the apo-state (PDB 1MWK) were required to dock it into the reconstruction of the open state at the available resolution (Figure 5G). To get a better fit of the ParM crystal structure into the map of the closed state (Figure 5A), we cleaved the apo-crystal structure of ParM across the hinge region into the two major domains (domains I and II), breaking the bonds at the regions where the large change between the ADP and apo states occur (see Experimental Procedures). The best fit was achieved when the two domains were moved toward each other around the hinge by ~25° (Figure 5B). Exactly the same closing of the cleft was observed between the

apo and ADP (PDB 1MWM) states (Figure 5C) (van den Ent et al., 2002). We found that the docking of separate domains from the apo-crystal produced a slightly better fit than when the unperturbed ADP-state crystal structure was used.

Comparisons of the power spectra of the raw images with those obtained from the reconstructions (Figures 5D, 5E, 5H, and 5I) show good matches, and it can be seen that the power spectrum from the segments classified as closed is different from that obtained from the segments classified as open. For the closed ParM segments, the n = 3 layer line (Figure 5D, red arrow) is more prominent than the n = ± 1 layer lines (Figure 5D, blue and green arrows), while for the open ParM segments, all three layer lines have nearly equal intensity (Figure 5H, red blue and green arrows). This can be measured quantitatively, and the ratio of intensities between the n = 3 and n = 1 layer lines is 2.1 in the closed state (Figure 5D) and 1.0 in the open state (Figure 5H). A similar approach was used to validate our atomic models—the power spectra generated from both atomic models matched well the power spectra of the raw images as well as the power spectra derived from the reconstructions used for the modeling (Figures 5D, 5E, 5F, 5H, 5I, and 5J). To evaluate how well the atomic models reflect the features of the reconstructions we calculated the Fourier Shell Correlation (FSC) between the maps and the atomic models (Figure S1). The FSC curves reached a value of 0.5 (an arbitrary but conservative measure of the resolution limit) at almost exactly the same values that we previously determined for the resolution of these maps, giving further credibility to these resolution estimates.

In our previous work, we showed that there is no nucleotide exchange after ParM polymerization (Orlova et al., 2007), and under the conditions used, AMP-PNP should always be bound in the cleft. Despite the fact that in the presence of GMP-PNP ParM was shown to have its cleft closed (Popp et al., 2008), we observe ~20% of segments having the cleft open. We suggest that there is an equilibrium between the closed and the open state within the ParM filament. When either AMP-PNP or GMP-PNP is bound, the equilibrium is shifted toward the closed state, but a fraction of segments can still be found in the open state.

A detailed comparison of the atomic models of the closed and open states of the ParM filament (Figure 6) shows how protomer interfaces change between these two states. In the closed state, each ParM promoter makes three longitudinal contacts and one lateral contact with its neighbors (Figures 6A and 6B). In the open state (Figures 6C and 6D), the residues 161–164 and 271–274 of the upper protomer and the residues 212–217 of the lower protomer move away from each other (Figures 6A and 6C, red arrows). Also, the contact between the residues 298–300 of the upper protomer and residues 239–341 of the lower protomer is broken in the open state (Figures 6A and 6C, green arrows). Our atomic models predict that, upon opening of the nucleotide binding cleft, the ParM filament would be less stable than when it is in the closed state.

Both atomic models are in agreement with the recent mutagenesis data. It has been shown that point mutations of residues 33, 34, 36, and 40 completely abolish ParM polymerization (Salje and Lowe, 2008). In both ParM states, these residues lie at the interface between protomers (Figure 6, residues are marked as spheres). Mutation of residue K123, which is located in helix 4 of domain I of ParM (van den Ent et al., 2002), does not affect

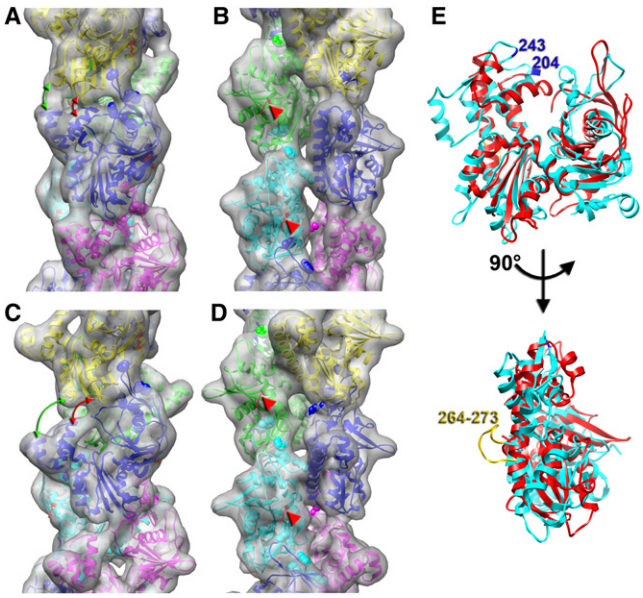

Figure 6. Detailed Views of the Two Structural States of the ParM Filament

(A and B) Pseudo-atomic model of the closed state is shown as ribbons, and the corresponding view of the model filtered to 10 Å resolution is shown as a transparent surface. The two views are related by 90° rotation around the helical axis.

(C and D) Pseudo-atomic model of the open state of the ParM filament. Red arrows mark the distances between residues 161–164 and 271–274 of the upper protomer, and the residues 212–217 of the lower protomer in both closed and open states. Green arrows mark the distances between residues 298–300 of the upper protomer, and residues 239–341 of the lower protomer in both structural states. Residues 33, 34, 36, and 40, which are crucial for filament maintenance, are shown as spheres in (A–D). Residue 123, involved in the interaction with ParR/ParC complex, is indicated in (A–D) with red arrowheads.

(E) A comparison between actin (cyan) and ParM (red) shows that while the cores of the two subunits are fairly well conserved, the peripheral regions in actin at the four "corners" of the subunit (responsible for protomer-protomer contacts in F-actin) have no correspondence with the secondary structural elements of ParM in these regions. Two residues (204 and 243) that have been implicated in actin polymerization (Rould et al., 2006) can be seen to be in a region that has no structural similarity in ParM. The hydrophobic plug on actin involves residues 264–273.

ParM polymerization but abolishes the interaction of ParM with the ParR/ParC complex. In our atomic models, this residue is located at the side of the filament (Figures 6A–D, red arrow heads), which would explain why this mutation does not alter ParM polymerization and why binding of ParR/ParC complex does not interfere with ParM polymerization. Both atomic models also show that the interfaces between protomers are completely different from that found in F-actin. This is consistent with the fact that there is no correspondence of secondary structural elements between ParM and actin (Figure 6E) in the regions of the actin subunit that are known to be involved in the filament interface. For example, mutation of actin residues 204 and 243 has been shown to abolish polymerization (Rould et al., 2006), but there is no structural similarity between ParM and actin in this region of the actin subunit (Figure 6E). Similarly, the "hydrophobic plug" in actin (residues 262–274) has been shown to be

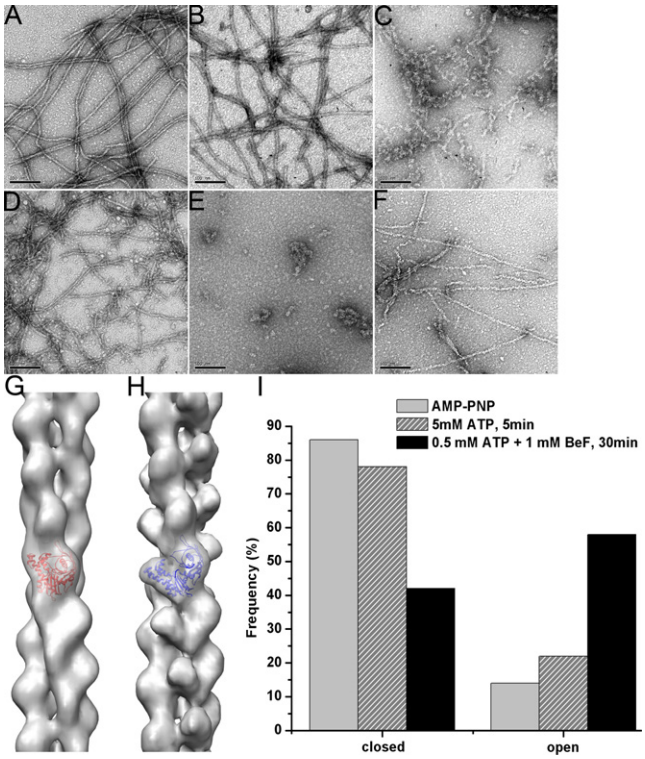

Figure 7. Structural Polymorphism of the ParM Filaments Depends on the Polymerization Conditions

EM micrographs of negatively stained ParM filaments formed at different conditions (A–F). Long filaments are formed in presence of AMP-PNP, and these filaments are stable even after several hours (A). In the presence of 5 mM ATP, shorter filaments are observed after 5 min of polymerization (B), and very few filaments along with aggregates are present after 30 min (C). After 5 min of polymerization in the presence of 0.5 mM ATP, ParM forms short filaments that tend to form bundles (D), while after 30 min, when all ATP is depleted, only amorphous aggregates are seen (E). Addition of 1 mM BeF to 0.5 mM ATP preserves some filaments even after 30 min incubation (F). Two structural states are found in negatively stained filaments—closed (G) and open (H). These states are shown as gray transparent surfaces with docked crystal structure of ParM in the closed (G, red ribbons) or open (H, blue ribbons) states. The frequency of these states within the filaments shown in (A), (B), and (F) is shown in (I).

essential for filament formation (Reisler and Egelman, 2007), but this element is completely missing from ParM (Figure 6E).

The Opening of the Cleft Is Coupled with ATP Hydrolysis

To elucidate the role of the two structural states of ParM filaments found, we imaged ParM filaments under several other conditions (Figure 7). We first determined that negative stain can be used to visualize the two different states. Although we found a smaller fraction of the open state of ParM in the negatively stained AMP-PNP-ParM (Figure 7A) sample (~10%), compared with the frozen hydrated filaments (~20%), the negatively stained reconstructions of the open (Figure 7H) and closed (Figure 7G) states of ParM were very similar at the available resolution to the cryo-EM reconstructions (Figures 5A and 5G, respectively).

When ParM was polymerized in the presence of a large molar excess (5.0 mM) of ATP (Figure 7B), we observed long and quite ordered filaments. These filaments disappeared over time as the ATP was consumed (Figure 7C). Image analysis revealed that over 20% of these ordered segments were in the open conformation (Figure 7I), suggesting that the opening of the nucleotide-binding cleft in ParM was associated with ATP hydrolysis (since ~10% of these segments had an open cleft with the nonhydrolyzable AMP-PNP). Using a lower concentration of ATP (0.5 mM) resulted in shorter filaments after 5 min of polymerization (Figure 7D), and almost no filaments were observed after 30 min (Figure 7E). The addition of BeF_3^-, used to mimic the ADP-Pi state in F-actin (Combeau and Carlier, 1988), rescues ParM filaments from depolymerization (Garner et al., 2004). When BeF_3^- was added shortly after polymerization at low ATP concentration (see Experimental Procedures), even after 30 min we observed long ParM filaments (Figure 7F). Interestingly, in comparison to AMP-PNP-filaments (Figure 7A), or ATP-filaments after short times (Figure 7B), BeF_3^--filaments (Figure 7F) had a quite different appearance, similar to the "ragged" morphology of F-actin after short times of polymerization (Steinmetz et al., 1997; Orlova et al., 2004). Cross-correlation sorting revealed that the majority of these segments were in the open state (Figure 7I), and showed that BeF_3^- stabilized the open conformation of the ParM subunits in the filament.

DISCUSSION

Nucleotide Preference of ParM

ParM is a member of the actin superfamily, which includes eukaryotic actins, actin-related proteins (ARPs), prokaryotic actin-like proteins (ALPs), chaperones (Hsc70 and DnaK), and sugar kinases (e.g., hexokinase). The family is defined by a shared nucleotide-binding motif called the "actin fold" (Bork et al., 1992) which, in all known cases, prefers ATP over GTP. For some family members, this preference is not strong. DnaK and some forms of hexokinase, for example, are only two- to four-fold more selective for ATP over GTP (Liberek et al., 1991). Most conventional eukaryotic actins bind 500–1000 times more tightly to ATP than GTP, although some actins are less discriminating. The best studied example of a weakly discriminating actin is that of budding yeast, which has only nine-fold greater affinity for ATP. In the presence of GTP, yeast actin assembles into filaments indistinguishable from ATP filaments, with a critical concentration only five-fold higher than in the presence of ATP (Wen et al., 2002). The difference in nucleotide selectivity between yeast and animal actins is due, in large part, to a single amino acid difference in the nucleotide binding pocket (Phe versus Tyr at position 305), a substitution that is widely conserved among fungi and plants and suggests a selective advantage for the ability to utilize GTP. van den Ent et al. (2002) also showed that the bacterial actin like protein MreB will polymerize in both ATP and GTP but did not determine nucleotide binding preference.

Popp et al. (2008) recently showed that ParM can also polymerize in the presence of GTP. Although these authors did not measure the relative affinities of ParM for different nucleotides, they suggested that, unlike other members of the actin superfamily, ParM prefers GTP over ATP and is "a predominantly GTP-driven molecular switch." To determine whether this is the case, we measured the affinities of ParM for ATP and GTP

by competition binding and found that, similar to yeast actin, ParM has a 10-fold higher affinity for ATP. Thus, at cellular ratios of ATP to GTP (generally >1.0), ParM will be predominantly ATP bound.

Popp et al. (2008) also report that, while ATP ParM filaments undergo dynamic instability, rapid shortening of filaments is often terminated by "rescue," and the filaments rarely or never completely disassemble. In contrast, they report that, upon switching from elongation to shortening, GTP ParM filaments disassemble completely. We also compared the assembly dynamics of ATP and GTP ParM using bulk light scattering assays and TIRF microscopy. In agreement with Popp et al. (2008), we find that the apparent critical concentrations of ATP and GTP ParM are identical, suggesting that the filaments have a similar stability, and by use of TIRF microscopy, we find no difference in the behavior of individual GTP and ATP ParM filaments. Both elongate bidirectionally and, upon switching to disassembly, both depolymerize completely. Some discrepancies between our results and those of Popp et al. (2008) are likely due to the fact that Popp et al. (2008) performed TIRF experiments on large filament bundles generated by a crowding agent, polyvinyl alcohol. The difference in the state of the protein under the two different imaging conditions is dramatic. Under our conditions, almost all observed filaments are short (<3 μM), uniform in intensity, unbranched, and highly dynamic. Electron microscopy of filaments prepared under these conditions confirms that fewer than 2% are associated with other filaments (Garner et al., 2004; Choi et al., 2008). In Popp et al. (2008), almost all observed filaments are >5 μm in length, of variable fluorescence intensity, and often display branching or fraying at the ends, typical of filament bundles. Lateral interactions within a large bundle could act to stabilize filaments, and it is possible that GTP filaments have a lower propensity to form tight bundles than ATP filaments. This, however, cannot explain all the discrepancies between our results. In a previous study, we used methylcellulose to form long, stable bundles of ATP ParM filaments between particles coated with ParR/parC complexes. When we cut the bundles in the middle to expose ADP filament ends, both halves of the bundle completely disassembled, despite the presence of the crowding agent. Another potential source of difference could be our fluorescent labeling protocols. Popp et al. (2008) use ParM labeled randomly with multiple rhodamine molecules on surface-exposed lysines. In our hands, rhodamine-labeled ParM has a dramatically enhanced tendency to bundle, even in the absence of crowding agents (data not shown). In our TIRF experiments, we used ParM labeled with a single Alexa-488 on an engineered C-terminal cysteine. Our data disagree with the view that ParM is "a predominantly GTP-driven molecular switch" and support the idea that, like other members of the actin superfamily, ParM is a preferential ATPase with the capacity to bind GTP, albeit with a lower affinity.

Equilibrium Between Open and Closed States of the ATP-Binding Cleft Is Common to Proteins of the Actin Superfamily

A number of papers have proposed an atomic model of the ParM filament (van den Ent et al., 2002; Orlova et al., 2007; Popp et al., 2008). We think that the structural heterogeneity within the ParM filament precludes the formulation of a single atomic model for the ParM filament. The majority of segments in the presence of AMP-PNP have subunits with a closed cleft, and the atomic model derived from this state is consistent with the recently published ParM model (Popp et al., 2008). The second structural state, where protomers have their cleft open to the same extent as seen in the apo crystal structure of ParM (van den Ent et al., 2002), is also present in filaments, even though the same nucleotide (AMP-PNP) is believed bound to both states. The evidence for a bound nucleotide in both states comes from the observation (Orlova et al., 2007) that there is no appreciable exchange of nucleotide in these filaments. The notion that a bound ligand may bias a distribution of states of a protein, rather than simply determining the conformation, has been described in many other systems. For example, it has been shown that there is an equilibrium between the discrete positions of tropomyosin on F-actin that is shifted by Ca^{2+}, as opposed to being directly linked to the divalent cation (Pirani et al., 2005).

The two structural states of ParM that we observe are very similar to the two states previously visualized by crystallography (van den Ent et al., 2002), and support the notion that all members of the actin superfamily can undergo large domain-domain motions (Bork et al., 1992). Recent observations of another bacterial actin homolog, AlfA, suggest that the subunits within the AlfA filament are mainly in an open conformation (Polka et al., 2009). It has been suggested that the opening of the nucleotide binding cleft in F-actin is coupled with ATP hydrolysis (Belmont et al., 1999). Within crystals of G-actin, the binding of ATP or ADP does not change the opening of the cleft (Rould et al., 2006), but it is possible that crystal-packing interactions may trap actin in the closed state. We have found both states of an actin subunit coexisting in actin filaments—the canonical state has the ATP-binding cleft closed (Galkin et al., 2008), while in the tilted state of F-actin the cleft is open (Galkin et al., 2002; Orlova et al., 2007). This suggests that in the mature actin filament, containing ADP-bound protomers, there is an equilibrium between the two states. While this equilibrium is shifted toward the closed state, ADP-protomers having their cleft open can still be found in actin filaments.

The Closed State of the Cleft Is Required but Not Sufficient for ParM Polymerization

Actin can form filaments in presence of ATP, ATP analogs, ADP, and even without any nucleotide bound, so modifications to impair its ability to polymerize, or cocomplexes with other proteins, are required for the crystallization of actin. This is consistent with the very small differences between the nonpolymerizable ATP-bound and ADP-bound crystals of actin that mainly involve subtle movement of the sensor loop (Rould et al., 2006). Is the opening of the ATP-binding cleft in ParM coupled with ATP hydrolysis? In contrast to actin, ParM can polymerize only in the presence of NTP, or NTP analogs such as AMP-PNP or GMP-PNP. This suggests that ParM monomers that have ATP bound are structurally different from ADP-ParM monomers. A crystal structure of nonpolymerizable ATP-ParM is required to understand what precludes ADP-ParM from forming filaments.

It was shown that BeF_3^- stabilizes actin filaments by mimicking the ADP-Pi state of the filament (Combeau and Carlier, 1988). Interestingly, BeF_3^- can rescue ParM filaments from the

fast depolymerization that occurs upon ATP hydrolysis but does not promote filament elongation (Garner et al., 2004). Our EM observations show the stabilization of the preformed ParM filaments by BeF_3^- after the depletion of ATP (Figures 7D–7F). Together, these results imply the existence of at least two structural states of the ParM monomers—one structural state allows them to polymerize, while the other state can occur only in the preformed filament, and monomers in this state can not spontaneously polymerize. We found that in the presence of BeF_3^- after the depletion of ATP the majority of segments had the cleft widely open (Figure 7I). This strongly suggests that the open state of the ParM filament is the dominant form in the ADP-Pi state, but monomers with the open cleft can not support elongation or form new filaments. The closed state of the cleft is required but not sufficient for ParM polymerization.

In the model proposed by Popp et al. (2008), both the GTP- and GDP-bound ParM monomers in a filament adopt a similar "closed" conformation. When GDP ParM monomers are exposed at the end of a filament, the loss of nucleotide causes a change in conformation from the "closed" to the "open" state and promotes monomer dissociation. That is, catastrophic shortening requires that the terminal ParM monomer in the filament be in the nucleotide-free or apo form. The requirement that the rapidly dissociating monomers are nucleotide-free appears to be based entirely on the fact that in the crystal structures solved by the Lowe group, ADP ParM appears in a closed conformation while apo ParM is open. We find that ParM filaments contain monomers in both the open and closed form and that the relative amounts in each form depend on the nucleotide bound. Thus, there is no need to invoke the existence of apo ParM monomers to explain a conformational change-driven increase in the rate of monomer dissociation from filament ends. Furthermore, we previously (Garner et al., 2004) found that addition of exogenous ADP to preformed ParM filaments increased their rate of disassembly. The best explanation for this observation is that, as in conventional actin (Teubner and Wegner, 1998), the terminal monomers of a ParM filament can exchange bound nucleotide with nucleotides in solution. If ADP ParM monomers were more stable than apo monomers, the addition of excess ADP should slow down dissociation rather than accelerate it.

The Opening of the ATP-Binding Cleft May Be Required for Phosphate Release

After short times of polymerization, when F-actin hydrolyzes ATP and releases the inorganic phosphate, filaments have a ragged morphology that evolves over time into more ordered filaments (Steinmetz et al., 1997; Orlova et al., 2004). This ragged morphology coincides with the increased number of actin protomers in the tilted state (Galkin et al., 2002; Orlova et al., 2004). In the tilted state, F-actin has its cleft open and lacks one of its longitudinal contacts (Galkin et al., 2002; Orlova et al., 2004). These observations explain why young actin filaments are less stable than aged ones (Kueh et al., 2008). In the mature frozen hydrated actin filaments, the majority of segments are in the closed state (Orlova et al., 2007), which is consistent with the closed cleft observed in the crystal structure of ADP-G-actin (Rould et al., 2006). This suggests that in F-actin the opening of the cleft is coupled with ATP hydrolysis, and once this process is completed the cleft closes.

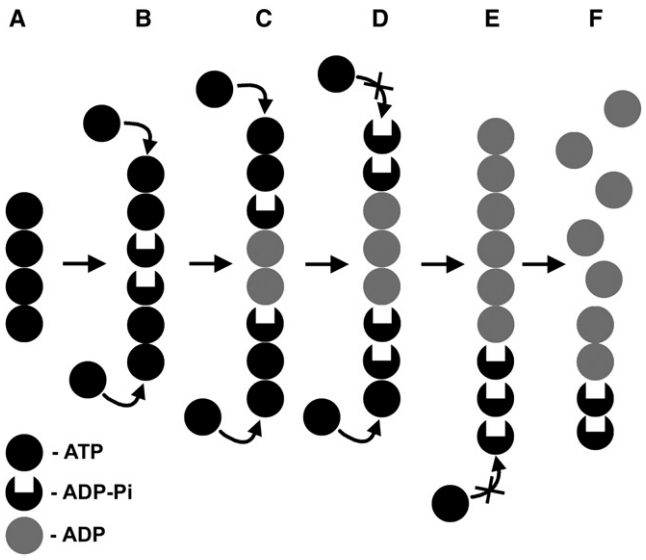

Figure 8. Model for the Dynamic Instability of ParM Filaments

ParM filament is shown as a stack of circles, where each circle represents a ParM protomer. Black circles represent ParM-ATP; gray circles represent ParM-ADP, and black circles with deleted center stand for the intermediate ParM-ADP-Pi state. Shortly after polymerization, ParM filament is composed of ATP subunits (A), which over time turn into ADP-Pi state (B) followed by the ADP state (C). The integrity of the filament in (A–C) is preserved by the ATP-cap. Inorganic phosphate release inhibits the formation of the protective ATP-cap (D). Finally, the ADP subunits are exposed (E), and the filament depolymerizes (F).

Stabilization of ParM filaments with BeF_3^- provides insight into what happens to protomers upon ATP hydrolysis. We show here that ParM protomers in the ADP-Pi state (mimicked by BeF_3^-) are mainly in the open form. Importantly, ParM filaments that are stabilized with BeF_3^- after ATP depletion a have ragged morphology (Figure 7F) similar to that observed in young actin filaments. Since actin and ParM have a substantial structural homology in the ATP-binding cleft region, we suggest that the opening of the ATP-binding cleft in the tilted state of F-actin, similar to what is seen with ParM, reflects the ADP-Pi state.

Why is ParM, in contrast to F-actin, dynamically unstable? We may speculate that once the inorganic phosphate is released, the cleft in F-actin closes and it returns to the stable conformation. ParM is structurally homologous to actin only in the core region, while it is very different from F-actin in the regions of subunit-subunit contacts within the filament. This explains why ParM forms left-handed two-start helices with contacts between the protomers that are absolutely unrelated to the contacts observed in F-actin (Figure 6). It is possible that because of this difference, the cleft in ParM can not be closed upon phosphate release, and protomers can not switch back to the closed state. The open conformation of ParM that we describe as the ADP-Pi state is an intermediate state between the stable ATP-filament and highly unstable ADP-filament. ParM filaments shrink from the ends (Garner et al., 2004). The structural alterations in the ParM filament that arise from the opening of the cleft in the ADP-Pi state preclude the addition of ATP-bound protomers to the ends of the filament, and thus prevent the formation of the protective ATP caps (Figure 8). The structural changes in

ParM that accompany Pi release are inconsistent with filament existence.

Implications for ParR/ParC Binding

Atomic models derived from both open and closed states are consistent with the mutagenesis data (Salje and Lowe, 2008) and place the ParR/ParC-binding site on the side of the ParM filament. We suggest that alteration of the side of the filament upon ATP hydrolysis allows the ParR/ParC complex to sense the nucleotide state of the filament and remain attached to subunits within the ATP cap. Since filaments capped with the ParR/ParC complex are stable and can grow to be long in the cell (Campbell and Mullins, 2007), it is likely that interaction of the ParR/ParC complex with the side of the filament may stabilize the ATP cap.

EXPERIMENTAL PROCEDURES

Sample Preparation and Electron Microscopy

ParM protein was overexpressed and purified as described elsewhere (Orlova et al., 2007). ParM in 30 mM Tris-HCL (pH 7.5), 0.1 M KCL, 2 mM $MgCl_2$, and 1 mM DTT was diluted to 3–-4 μM, and polymerized by the addition of AMP-PNP (5 mM) or GMP-PNP (5 mM); after 5–10 min incubation, 5 μl was applied to glow-discharged carbon-covered 300-mesh copper grids. Alternatively, polymerization was started by the addition of 100 μM–5 mM ATP. For ADP-P_i state, 1 mM $BeSO_4$ and 5 mM NaF were added after 2–4 min of polymerization. The mixture was incubated up to 15–30 min at room temperature.

The grids were either negatively stained with 1% (w/v) uranyl acetate or blotted and plunged into liquid ethane. Images were collected on film using a Tecnai 12 (80 kV and ×30,000 magnification) for negatively stained samples or a Tecnai 20 FEG (200 kV and ×50,000 magnification) for frozen-hydrated samples. The 31 different images used for the cryo-EM reconstruction had defocus values ranging from 2.0 to 4.0 μm. Films were scanned on a Nikon Coolscan 8000 with a sampling of 4.16 Å per pixel for negative-stain images and 2.38 Å per pixel for cryo-EM.

Image Analysis

The SPIDER package (Frank et al., 1996) was used for most image processing, but the BSOFT package (Heymann and Belnap, 2007) was used to determine the defocus values in the micrographs while EMAN (Ludtke et al., 1999) package was used to extract filament images from micrographs.

Image Analysis of Frozen Hydrated AMP-PNP-ParM-Filaments

All cryo-EM images were multiplied by the theoretical CTF to correct for phase reversals and to optimize the signal-to-noise ratio. Final reconstructions were then divided by the weighted sum of the squared CTFs and corrected for the envelope function of the EM with the use of negative B-factors. The segments were classified as shown in Figure 4A. First, a global reconstruction was generated using all segments (n = 18,870). The crystal structure of the closed state of ParM (PDB entry 1MWK) was docked into the global map using the UCSF Chimera software (Pettersen et al., 2004), and subsequently used to generate a model filament in the closed state. The ParM crystal structure in the open state (PDB entry 1MWK) was used to generate a model filament having the cleft open. The position of the first domain of ParM in the closed and the open states models were identical, so the only difference was the opening of the cleft and the breakage of the contact between the protofilaments (Figure 6, red and green arrows). These models were used as references for an initial sorting (Figure 4A). These two reference volumes were scaled to 4.76 Å per pixel and projected into 100 × 100-pixel images with an azimuthal rotational increment of 4°, generating 180 reference projections (2 × 90). The ParM segments were down-sampled to 4.76 Å per pixel and cross-correlated with the 180 reference projections. Reconstructions were independently generated from the two classes of segments—closed (n = 12,523), and open (n = 3,374). The validity of the sorting was confirmed by two independent means. First, power spectra of segments from both classes were indistinguishable from the power spectra of the 3D reconstructions (Figure 5). Second, we used the IHRSR approach (Egelman, 2000) to show the convergence of the two classes to their unique solutions independently form the starting point (Figure S2). The 3D reconstruction of the open set yielded symmetry of 165°/24.2Å and was used to build up an atomic model of the ParM filament in the open state (Figures 6C and 6D). The closed set was sorted by the twist and the axial rise. Five model volumes were created by imposing five corresponding symmetries on the crystal structure of ParM in the closed state (PDB entry 1MWM). The symmetries were chosen to keep the pitch of the three-start helix fixed at 1/194 $Å^{-1}$ as follows: 160.7°/21.87Å, 163°/23.11Å, 165.2°/24.3Å, 167.5°/25.51Å, and 169.7°/26.73Å. These five volumes were scaled to 4.76 Å per pixel and projected into 100 × 100-pixel images with an azimuthal rotational increment of 4°, generating 450 reference projections (5 × 90). The ParM segments were down-sampled to 4.76 Å per pixel and cross-correlated with the 450 reference projections. The power spectra of segments from three largest bins were calculated (Movie S1), and behave exactly as predicted by the twist and axial rise values shown in the histogram (Figure 4B). Second, we used the IHRSR approach to separately reconstruct these three bins, and each class converged to the expected symmetry (Figures 4C and 4D). The reconstruction form the largest class number 3 (n = 3,611) iterated at the original scale of 2.38 Å per pixel yielded the symmetry of 165.2°/24.3Å, and was used to build up an atomic model of the ParM filament in the closed state (Figures 6A and 6B).

To validate our maps, we iterated each set from the two very different symmetries to check the convergence of the set to the same solution (Figure S2). We observed a nice convergence to the same solution within each set. Our extensive work with IHRSR package proved that heterogeneous sets would never generate the same 3D reconstruction if iterated from the different starting points. Also, to avoid model biasing, both sets were reconstructed starting from a features solid cylinder (Figure S2).

The conservative FSC = 0.5 criterion was used for resolution determination. A widely used approach has been to split an aligned data set into two halves yielding two volumes for FSC comparison, but this method can yield an overly optimistic resolution value due to alignment of noise. To avoid that, we divided the images into two sets and then used the IHRSR procedure on these two sets starting each from a different helical symmetry. The two structures converge to a common symmetry, and the resultant volumes did not have noise aligned to a common reference. However, the smaller number of images present in each half data set would underestimate the resolution in the combined reconstruction, under conditions where the resolution was likely to be limited by the number of particles. Thus, the 17.2 Å resolution that was measure by this method in our closed map, and the 19.5 Å resolution determined for the open state, were the most pessimistic resolution estimations.

Image Analysis of Negatively Stained Samples

We extracted 10,181 overlapping segments of negatively stained AMP-PNP ParM filaments, and 11,173 segments prepared in presence of GMP-PNP, each 416 Å in length. First, a global reconstruction of each set was generated using all segments. After 60 cycles of IHRSR refinement, the AMP-PNP set yielded a stable solution of 165.2°/24.7 Å (Figure 1B, gray surface), while the GMP-PNP set converged to 165.3°/24.7 Å (Figure 1C, gray surface). This global reconstruction of the AMP-PNP set was then deformed into nine different twist states ranging from 157 to 173° with a step of 2°, and these models were used as references for the twist sorting (Figures 1G–1I).

We selected 4,726 segments of ParM formed in the presence of 0.5 mM ATP after 5 min of polymerization. Similarly to the frozen hydrated sample, segments were divided into the two classes on the basis of the opening of the nucleotide binding cleft. The majority of segments (n = 3,680) had the better correlation with the closed cleft reference, and yielded an IHRSR reconstruction shown in (Figure 7G) with the symmetry of 165.2°/24.7 Å. The smaller set that represented the open state subset (n = 1,046) converged to 164.8°/24.8 Å symmetry.

Filaments formed in presence of 0.5 mM ATP and subsequently stabilized with the addition of 2 mM BeF_3^- possessed a ragged morphology (Figure 7F). We selected only segments that were straight within the 416 Å long box, which was the length of the segments used in IHRSR procedure. Thus, only 1,070 segments were selected and sorted into two classes on the basis of the structural state. More than half of the images (n = 599) were assigned to the open state class and yielded a reconstruction shown in (Figure 7H), having the symmetry of 165.4°/24.7 Å. The smaller subset that represented the closed state converged to 164.8°/24.9 Å symmetry.

ACCESSION NUMBERS

Coordinates of the atomic models have been deposited in the PDB with accession codes 3IKY (open state) and 3IKU (closed state). Reconstruction volumes have been deposited with the EMDB with accession codes EMD-5129 (open state) and EMD-5128 (closed state).

SUPPLEMENTAL DATA

Supplemental data include one movie and two figures and can be found with this article online at http://www.cell.com/structure/supplemental/S0969-2126(09)00291-3.

ACKNOWLEDGMENTS

This work was supported by NIH GM081303 (E.H.E.) and GM61010 (R.D.M.)

Received: May 22, 2009
Revised: July 8, 2009
Accepted: July 9, 2009
Published: September 8, 2009

REFERENCES

Belmont, L.D., Orlova, A., Drubin, D.G., and Egelman, E.H. (1999). A change in actin conformation associated with filament instability after Pi release. Proc. Natl. Acad. Sci. USA *96*, 29–34.

Bork, P., Sander, C., and Valencia, A. (1992). An ATPase domain common to prokaryotic cell cycle proteins, sugar kinases, actin, and hsp70 heat shock proteins. Proc. Natl. Acad. Sci. USA *89*, 7290–7294.

Campbell, C.S., and Mullins, R.D. (2007). In vivo visualization of type II plasmid segregation: bacterial actin filaments pushing plasmids. J. Cell Biol. *179*, 1059–1066.

Choi, C.L., Claridge, S.A., Garner, E.C., Alivisatos, A.P., and Mullins, R.D. (2008). Protein-nanocrystal conjugates support a single filament polymerization model in R1 plasmid segregation. J. Biol. Chem. *283*, 28081–28086.

Combeau, C., and Carlier, M.F. (1988). Probing the mechanism of ATP hydrolysis on F-actin using vanadate and the structural analogs of phosphate BeF-3 and A1F-4. J. Biol. Chem. *263*, 17429–17436.

Egelman, E.H. (2000). A robust algorithm for the reconstruction of helical filaments using single-particle methods. Ultramicroscopy *85*, 225–234.

Egelman, E.H. (2007). The iterative helical real space reconstruction method: surmounting the problems posed by real polymers. J. Struct. Biol. *157*, 83–94.

Egelman, E.H., and DeRosier, D.J. (1982). The Fourier transform of actin and other helical systems with cumulative random angular disorder. Acta Crystallogr. A *38*, 796–799.

Flyvbjerg, H., Jobs, E., and Leibler, S. (1996). Kinetics of self-assembling microtubules: an "inverse problem" in biochemistry. Proc. Natl. Acad. Sci. USA *93*, 5975–5979.

Frank, J., Radermacher, M., Penczek, P., Zhu, J., Li, Y., Ladjadj, M., and Leith, A. (1996). SPIDER and WEB: Processing and visualization of images in 3D electron microscopy and related fields. J. Struct. Biol. *116*, 190–199.

Galkin, V.E., Orlova, A., Cherepanova, O., Lebart, M.C., and Egelman, E.H. (2008). High-resolution cryo-EM structure of the F-actin-fimbrin/plastin ABD2 complex. Proc. Natl. Acad. Sci. USA *105*, 1494–1498.

Galkin, V.E., VanLoock, M.S., Orlova, A., and Egelman, E.H. (2002). A new internal mode in F-actin helps explain the remarkable evolutionary conservation of actin's sequence and structure. Curr. Biol. *12*, 570–575.

Garner, E.C., Campbell, C.S., and Mullins, R.D. (2004). Dynamic instability in a DNA-segregating prokaryotic actin homolog. Science *306*, 1021–1025.

Garner, E.C., Campbell, C.S., Weibel, D.B., and Mullins, R.D. (2007). Reconstitution of DNA segregation driven by assembly of a prokaryotic actin homolog. Science *315*, 1270–1274.

Gerdes, K., and Molin, S. (1986). Partitioning of plasmid R1. Structural and functional analysis of the parA locus. J. Mol. Biol. *190*, 269–279.

Heymann, J.B., and Belnap, D.M. (2007). Bsoft: image processing and molecular modeling for electron microscopy. J. Struct. Biol. *157*, 3–18.

Jensen, R.B., and Gerdes, K. (1997). Partitioning of plasmid R1. The ParM protein exhibits ATPase activity and interacts with the centromere-like ParR-parC complex. J. Mol. Biol. *269*, 505–513.

Kueh, H.Y., Brieher, W.M., and Mitchison, T.J. (2008). Dynamic stabilization of actin filaments. Proc. Natl. Acad. Sci. USA *105*, 16531–16536.

Liberek, K., Skowyra, D., Zylicz, M., Johnson, C., and Georgopoulos, C. (1991). The *Escherichia coli* DnaK chaperone, the 70-kDa heat shock protein eukaryotic equivalent, changes conformation upon ATP hydrolysis, thus triggering its dissociation from a bound target protein. J. Biol. Chem. *266*, 14491–14496.

Lowe, J., and Amos, L.A. (2009). Evolution of cytomotive filaments: The cytoskeleton from prokaryotes to eukaryotes. Int. J. Biochem. Cell Biol. *41*, 323–329.

Ludtke, S.J., Baldwin, P.R., and Chiu, W. (1999). EMAN: semiautomated software for high-resolution single-particle reconstructions. J. Struct. Biol. *128*, 82–97.

Moller-Jensen, J., Borch, J., Dam, M., Jensen, R.B., Roepstorff, P., and Gerdes, K. (2003). Bacterial mitosis: ParM of plasmid R1 moves plasmid DNA by an actin-like insertional polymerization mechanism. Mol. Cell *12*, 1477–1487.

Nishida, E., and Sakai, H. (1983). Kinetic analysis of actin polymerization. J. Biochem. *93*, 1011–1020.

Nordstrom, K., Molin, S., and Agaard-Hansen, H. (1980). Partitioning of plasmid R1 in *Escherichia coli*. I. Kinetics of loss of plasmid derivatives deleted of the par region. Plasmid *4*, 215–227.

Oda, T., Iwasa, M., Aihara, T., Maeda, Y., and Narita, A. (2009). The nature of the globular- to fibrous-actin transition. Nature *457*, 441–445.

Orlova, A., Garner, E.C., Galkin, V.E., Heuser, J., Mullins, R.D., and Egelman, E.H. (2007). The structure of bacterial ParM filaments. Nat. Struct. Mol. Biol. *14*, 921–926.

Orlova, A., Shvetsov, A., Galkin, V.E., Kudryashov, D.S., Rubenstein, P.A., Egelman, E.H., and Reisler, E. (2004). Actin-destabilizing factors disrupt filaments by means of a time reversal of polymerization. Proc. Natl. Acad. Sci. USA *101*, 17664–17668.

Pettersen, E.F., Goddard, T.D., Huang, C.C., Couch, G.S., Greenblatt, D.M., Meng, E.C., and Ferrin, T.E. (2004). UCSF Chimera–a visualization system for exploratory research and analysis. J. Comput. Chem. *25*, 1605–1612.

Pirani, A., Xu, C., Hatch, V., Craig, R., Tobacman, L.S., and Lehman, W. (2005). Single particle analysis of relaxed and activated muscle thin filaments. J. Mol. Biol. *346*, 761–772.

Polka, J., Kollman, J.M., Agard, D.A., and Mullins, R.D. (2009). The structure and assembly dynamics of a plasmid actin, AlfA, imply a novel method of DNA segregation. J. Bact., in press.

Popp, D., Narita, A., Oda, T., Fujisawa, T., Matsuo, H., Nitanai, Y., Iwasa, M., Maeda, K., Onishi, H., and Maeda, Y. (2008). Molecular structure of the ParM polymer and the mechanism leading to its nucleotide-driven dynamic instability. EMBO J. *27*, 570–579.

Reisler, E., and Egelman, E.H. (2007). Actin structure and function: what we still do not understand. J. Biol. Chem. *282*, 36133–36137.

Rould, M.A., Wan, Q., Joel, P.B., Lowey, S., and Trybus, K.M. (2006). Crystal structures of expressed non-polymerizable monomeric actin in the ADP and ATP states. J. Biol. Chem. *281*, 31909–31919.

Salje, J., and Lowe, J. (2008). Bacterial actin: architecture of the ParMRC plasmid DNA partitioning complex. EMBO J. *27*, 2230–2238.

Steinmetz, M.O., Goldie, K.N., and Aebi, U. (1997). A correlative analysis of actin filament assembly, structure and dynamics. J. Cell Biol. *138*, 559–574.

Teubner, A., and Wegner, A. (1998). Kinetic evidence for a readily exchangeable nucleotide at the terminal subunit of the barbed ends of actin filaments. Biochemistry *37*, 7532–7538.

van den Ent, F., Moller-Jensen, J., Amos, L.A., Gerdes, K., and Lowe, J. (2002). F-actin-like filaments formed by plasmid segregation protein ParM. EMBO J. *21*, 6935–6943.

Wen, K.K., Yao, X., and Rubenstein, P.A. (2002). GTP-yeast actin. J. Biol. Chem. *277*, 41101–41109.

